Materials Science & Engineering A 944 (2025) 148885

Contents lists available at ScienceDirect

Materials Science & Engineering A

journal homepage: www.elsevier.com/locate/msea

Influence of roughness and subsurface porosity on the fatigue life of AlSi10Mg produced by Laser Powder Bed Fusion

Camille van der Rest [a,*], Rodrigo Arturo Manzano Navarrete [a,b], Aude Simar [a], Olivier Poncelet [a]

[a] Université Catholique de Louvain (UCLouvain), Institute of Mechanics, Materials and Civil Engineering (iMMC), IMAP, Place Sainte-Barbe 2, bte L5.02.02, B-1348, Louvain-La-Neuve, Belgium

[b] Lehigh University, Department of Mechanical Engineering & Mechanics, 19 Memorial Drive West, Bethlehem, 18015, PA, United States

ARTICLE INFO

Keywords:
Fatigue
Laser powder bed fusion
AlSi10Mg
Contouring
Roughness
Keyhole porosity
Post-processing

ABSTRACT

Porosity and poor surface quality are critical defects in Laser Powder Bed Fusion (L-PBF) that significantly impact mechanical performance, particularly under cyclic loading. To enhance fatigue resistance without relying on time-consuming post-processing, process optimization is essential. This study investigates the influence of roughness and subsurface porosity on the fatigue behavior of net-shaped, vertically built AlSi10Mg samples by tailoring contour parameters. Three sample sets were intentionally produced: (i) with a rough surface, (ii) with a smooth surface, and (iii) with a smooth surface and subsurface keyhole pores. Each set was evaluated in different conditions: as-built, mirror-polished, and sandblasted. Results show that optimizing contour strategies improves fatigue life but remains insufficient on its own. Post-processing, particularly sandblasting, significantly enhances fatigue performance. Surprisingly, subsurface keyhole pores do not appear to be as detrimental as surface roughness in fatigue failure. However, lack-of-fusion defects, when present near the surface, are critical stress concentrators and can drastically reduce fatigue life. These findings emphasize the critical role of surface state in fatigue behavior and provide insights for L-PBF process optimization in high-performance applications.

1. Introduction

Originally conceived as a rapid prototyping technology, Laser Powder Bed Fusion (L-PBF) has become a technology capable of producing fully functional engineering components. Research and development into feedstock materials and process characteristics has led to its adoption in a wide range of industries, including transportation, aerospace, pharmaceutical, sports, energy, and construction [1,2]. Among the different materials used in L-PBF, aluminum-silicon (Al-Si) alloys stand out due to their improved melting characteristics, making them attractive in lightweight structural applications [3,4]. The most widely used alloy in this family is AlSi10Mg, which has a hierarchical, multi-scale microstructure and static properties comparable (if not better than) those of cast aluminum alloys [5–7]. Despite its good static properties, one major mechanical limitation of AlSi10Mg lies in its fatigue properties. Research shows that, compared to wrought Al6061, the fatigue endurance of AlSi10Mg was approximately one order of magnitude lower for the same stress level. This low fatigue resistance can be attributed mainly to porosity and high side surface roughness. These defects which arise during manufacturing have a first-order impact in fatigue resistance, as they become sites for stress concentration and crack nucleation [7,8].

In recent years, researchers have tried to understand the complex formation mechanisms and impact of porosity and roughness on the fatigue properties of AlSi10Mg. As a result, different contributing factors such as the process parameters (e.g. laser power, scanning speed) [9–11], build orientation [12,13], scanning strategy [14–16], track stability [17,18] have been identified as having a first-order impact in the generation of defects during the L-PBF process. To mitigate the detrimental effect of defects and improve fatigue performance, a traditional research roadmap focuses on the use of mechanical and/or thermal post-processing. In this context, the effect of sandblasting [19,20], shot-peening [21,22], friction stir processing [23], hot isostatic pressing [24], and combinations of machining and polishing with T5 and T6 heat treatments [25–27] have been studied. These research studies show that treatments that are able to reduce surface roughness and irregular

* Corresponding author.
E-mail address: camille.vanderrest@uclouvain.be (C. van der Rest).

https://doi.org/10.1016/j.msea.2025.148885
Received 24 April 2025; Received in revised form 15 July 2025; Accepted 26 July 2025
Available online 28 July 2025
0921-5093/© 2025 The Authors. Published by Elsevier B.V. This is an open access article under the CC BY-NC-ND license (http://creativecommons.org/licenses/by-nc-nd/4.0/).

porosity within the bulk have a positive impact on fatigue life. However, this improvement comes at the expense of incurring time-consuming treatments that negate the ready-to-use advantage of L-PBF.

An alternative approach consists in the optimization of the process parameters during L-PBF in order to prevent the emergence of defects. Studies have shown that porosity is linked to the energy input. While an insufficient amount of energy will lead to an improper melting and the emergence of irregular lack-of-fusion defects, an excessive amount of energy will lead to the local vaporization of material and entrapment of vapor bubbles in the melt pools, leading to round keyhole pores [28–30]. In a similar vein, the emergence of roughness has been linked to the energy input, track stability, and effect of the scanning strategy on the absorptivity of the powder bed. A process window that produces stable tracks, which have low viscosity and high wettability, will produce the lowest surface roughness [14,15,31].

Recent investigations have shown that a contour-first strategy combined with a level of Track Energy Density (TED) at the onset of keyholing produces the best surface finish [16], establishing a promising starting point for future fatigue investigations.

To assess the fatigue performance achieved through contour parameter optimization, it is essential to compare it with the effects of various post-processes. Previous studies [19–23,25,26,32,33] have primarily focused on individual or combined post-processing strategies to enhance fatigue resistance. Recent advancements have highlighted three key approaches:

- Microstructure refinement [34];
- Surface roughness reduction [35,36];
- Introduction of compressive residual stresses [37].

Studies on the fatigue behavior of AlSi10Mg indicate that the nature of the improvements depends on the dominant mechanism at play. Enhancing surface quality typically shifts the fatigue curve towards higher stress ranges [25,26,36]. Conversely, microstructural modifications [25,26], elimination of large pores [23] or introduction of compressive residual stresses [22,26] primarily reduce the material's sensitivity to stress, hence slope of the Wöhler curve.

The present paper proposes alternative L-PBF contour conditions, different from the core parameters, in order to intentionally produce three families of samples: rough, smooth, and smooth with subsurface pores. This careful selection of contour parameters aims to investigate the influence of roughness and subsurface porosity on the fatigue behavior of AlSi10Mg fabricated via L-PBF. Additionally, polishing and sandblasting were explored as surface post-processes, complementing a conventional stress-relief heat treatment. Comprehensive characterization of roughness and porosity was conducted, followed by static and cyclic mechanical testing to evaluate the impact of these factors on fatigue performance. The ultimate goal is the validation of the potential for improving fatigue life, by reducing roughness while creating subsurface porosity.

2. Materials and experimental procedure

2.1. Sample manufacturing

All the samples in this work were produced by Laser Powder Bed Fusion in a ProX 200 equipment from 3DSystems with a maximal laser power of 273.6 W (spot diameter = 75 μm). The manufacturing of samples was carried out using AlSi10Mg recycled metallic powder produced by TLS Technik. The particle size distribution ranges from 15 to 53 μm, and the particle morphology is spherical. The chemical composition was measured using inductively coupled plasma (ICP) and is provided in Table 1. In order to recycle the powder and remove large particles and conglomerates of particles, the powder was sieved using a 63 μm-mesh screen.

Net-shaped dog-bone cylindrical samples were manufactured vertically by L-PBF with a layer thickness of 30 μm. Schematic representation and dimensions (according to ASTM E8/E8M-15a and ASTM E466-15 standards) of the tensile and fatigue samples are provided in Fig. 1(a and b). The total length of the samples was 60 mm. Fig. 1(c) depicts the contour-first scanning strategy applied at each layer. The circular contour (thick line) was lased first with specific pre-optimized laser power and speed (see Table 2). Subsequently, the bulk zone was lased with parallel laser tracks (thin arrows) going back and forth. The orientation of these laser tracks was shifted by 90° between each layer. The offset between contour and bulk tracks was 60 μm, while the hatching distance between two successive bulk tracks was 100 μm.

Table 1
Chemical composition of AlSi10Mg powder.

Element	Al	Si	Mg	Fe
Mass Fraction (%)	Balance	10.02	0.32	0.11

Three families of samples were printed with constant L-PBF bulk parameters and various contour parameters in order to obtain different roughness and subsurface porosity states, as detailed in Table 2. Note that the sample's designation used throughout the present study corresponds to the relative power and speed of the contour parameters: 85–1200, 100–600, and 100–300 for the rough, smooth and smooth with keyhole pores, respectively.

2.2. Heat treatment and post-processing

A stress-relief heat treatment (SRHT) was carried out on all the tensile and fatigue samples to achieve residual stress relaxation without significantly altering the microstructure and mechanical properties. In order to remain as close to the as-built state as possible, this SRHT was performed at 250 °C for 2 h [39]. The heat treatment was carried out under argon using a Heraeus VT 5050 EKP oven.

Fatigue samples were tested in three conditions: stress relieved (SRHT), stress relieved and polished (SRHT + P), and stress relieved and sandblasted (SRHT + SB). Polishing was carried out in successive steps. First, samples were held in a Myford lathe (rotation speed = 150 rpm) and grinded with SiC sandpapers, then polished with diamond paste down to 0.25 μm. To eliminate detrimental circumferential scratches, longitudinal polishing was then performed by hand to reach R_a ~0.1 μm. This procedure removes approximately 100 μm to the diameter. Sandblasting was carried out for 1 min using a Laborex Type 1250 industrial cleaning and finishing machine. Samples were automatically rotated during sandblasting and the distance between the sand nozzle and the sample was kept at 10 cm. The sand was pink corundum LX 5200, made of 98 % of Al_2O_3, with d50 = 445 μm. The change in sample diameter is lower than 1 μm after sandblasting.

2.3. Characterizations

Roughness was characterized using the Keyence VHS 7000 series 3D digital microscope. 3D horizontal traveling serial recordings were performed over the surface of interest, parallel to the building direction (see dashed arrow in Fig. 1(c)), with a magnification of 150x. Following the guidelines of the EN ISO 4288 for surface roughness measurements, the low and high-pass filters (λs and λc, respectively), the assessment length (Ln) and the traveling length (Lt) used for the roughness measurements are provided in Table 3. The evaluated roughness parameters were the arithmetic average roughness (R_a), the maximum profile roughness (R_z), peak (R_p) and valley (R_v) roughnesses. The procedure was repeated six times for each sample, rotating the sample along its longitudinal axis between each measurement.

An in-depth characterization of the distribution and volume of porosity was carried out using X-Ray computed tomography (CT). An EasyTom XL CT scanner was used, with a voxel size of 2 μm. Processing of the tomography data was performed using Fiji software.

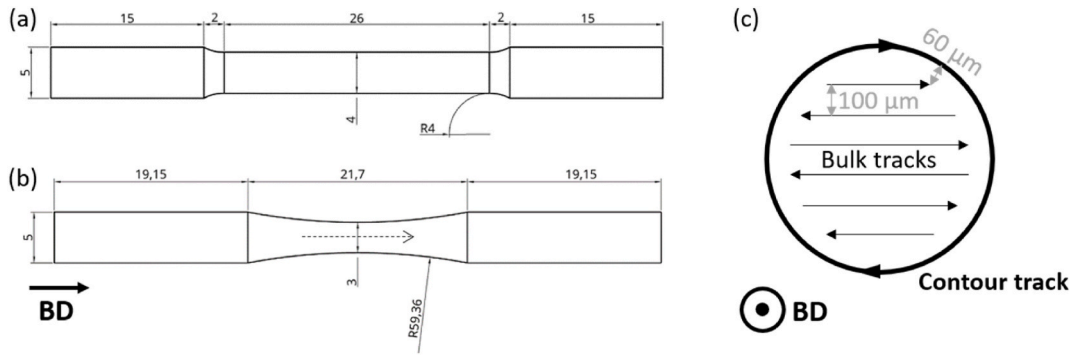

Fig. 1. (a) Dimensions of tensile samples in mm. (b) Dimensions of fatigue samples in mm. The dashed arrow represents the location of the roughness measurements (see Section 2.3). (c) Schematic representation (not to scale) of the L-PBF scanning strategy of a cross-section with the thick circle representing the contour track, lased first, and the thin lines representing bulk lasering with parallel back-and-forth tracks, lased after the contour. BD = building direction.

Table 2
Process parameters of the three families of samples: rough, smooth and smooth with keyhole pores (KHP). TED = Track Energy Density.

Families of samples	Bulk			Contour		
	Laser Power [W]	Scanning Speed [mm/s]	TED [J/m]	Laser Power [W]	Scanning Speed [mm/s]	TED [J/m]
85–1200 Rough				232.5	1200	194
100–600 Smooth	232.5	1200	194	273.6	600	456
100–300 Smooth with KHP				273.6	300	912

Table 3
Profile roughness measurement parameters following EN ISO 4288.

λs [µm]	8.0
λc [mm]	2.5
Ln [mm]	12.5
Lt [mm]	15.0

Conventional metallographic study and characterisation have been performed on cross-sections by optical microscopy (Keyence VHS 7000 series 3D digital microscope) and Scanning Electron Microscopy - SEM (Zeiss Ultra 55).

2.4. Mechanical testing

Uniaxial tensile tests were performed following ASTM E8/E8M-15a standard at room temperature. The tensile tests were carried out using a Zwick/Roell Instron® testing machine with a pre-loading of 5 N, a displacement rate of 1 mm/min, and gauge length of 20 mm. Two samples per condition were tested. Total fatigue life tests were performed following ASTM E466-15 standard at room temperature. Force controlled with constant amplitude uniaxial fatigue tests (tensile-tensile, R = 0.1) were carried out on an MTS Bionix 25 kN servo hydraulic testing machine until complete separation of the half-samples. Maximum stress levels between 140 MPa and 240 MPa were chosen based on the yield strength and at least twelve samples per condition were tested (distributed on five or six stress levels). The frequency was set at 30 Hz. If samples remained unbroken, fatigue tests were stopped at 1×10^7 cycles and qualified as run-outs, according to DIN EN 6072. Fracture surfaces were characterized with SEM. Total life curves were fitted with the Kohout-Věchet model [38], see Equation (1), while excluding run-outs.

$$\Delta\sigma = a \cdot \left(\frac{(N_f + B)\cdot C}{N_f + C}\right)^b \quad (1)$$

In Equation (1), $\Delta\sigma = \sigma_{max} - \sigma_{min}$ is the stress range [MPa], N_f is the number of cycles to failure [/] and a [MPa], b, B, and C [/] are fitting parameters determined by the least square method. This model allows the description of the fatigue curves over the whole fatigue range, from (very) low to (very) high cycle fatigue [38]. It was preferred to Basquin's fit, i.e. the classical power law model $\Delta\sigma = a \cdot (N_f)^b$, which is only applicable in the range of 10^3 to 10^6 cycles (linear fit in log-log scale) [38].

3. Results

3.1. Surface roughness

The roughness measurements (R_a, R_z, R_v, and R_p) for the three families of samples in stress-relieved (SRHT) and stress-relieved + sandblasted (SRHT + SB) conditions are presented in Table 4. Fig. 2 illustrates these values in two ways: the evolution of R_a as a function of the contour TED, as well as the comparison of the contributions of R_v and R_p, for both surface conditions.

For the SRHT condition and in the absence of surface treatment, increasing the contour TED allows to significantly decrease R_a and R_z, as mentioned in [16] and confirmed by Table 4. In the case of R_a, compared to a reference value of 9 µm, roughness values averaged 5 and 4.3 µm for the 100–600 and 100–300 samples, respectively. This represents a decrease in R_a of 44 % for the 100–600 and of 52 % for the 100–300 samples. R_z shows a trend similar to R_a, with a decrease of 53 % and 58 %, respectively. After sandblasting (SB), the roughness values of the 85–1200 samples decrease slightly, whereas they increase slightly for 100–600 and 100–300 samples, as shown in Fig. 2(a). This means that the low roughness levels achieved when optimizing the contour parameters (e.g. 100–600 and 100–300) cannot be further improved by using sandblasting as a surface post-process.

In addition, the roughness topology was studied by comparing the contributions of valleys and peaks, see Fig. 2(b). In the 85–1200 SRHT samples (top-right black point in Fig. 2(b)), R_p constitutes by 52 % to the total R_z, while R_v accounts for 48 % of R_z. Increasing the TED (following the black line in Fig. 2(b)) reduces both R_p and R_v, causing the overall reduction in R_z described above. However, this reduction is not proportional between R_p and R_v. As a result, R_v becomes higher than R_p and thus the main contributor to R_z, accounting for 64 % and 60 % of the total R_z in the 100–600 and 100–300 SRHT samples, respectively. From a physical point of view, increasing the contour TED reduces the amount of sintered, unmelted particles on the sample surface while having a

Table 4
Arithmetic average roughness (R_a), maximum profile roughness (R_z), valleys (R_v) and peaks (R_p) for the three families of samples. Comparison between stress-relieved (SRHT) and stress-relieved + sandblasted (SRHT + SB) samples.

	Contour TED [J/m]	Post-processing	R_a [μm]	R_z [μm]	R_v [μm]	R_p [μm]
85–1200 Rough	194	SRHT	9.0 ± 0.4	58.7 ± 3.1	28.1 ± 1.6	30.6 ± 1.5
		SRHT + SB	8.5 ± 1.6	49.9 ± 11.7	25.5 ± 4.4	24.4 ± 8.3
100–600 Smooth	456	SRHT	5.0 ± 0.7	27.5 ± 4.3	16.5 ± 2.4	11.0 ± 1.9
		SRHT + SB	5.4 ± 0.6	31.0 ± 4.2	17.2 ± 2.4	13.8 ± 1.5
100–300 Smooth with KHP	912	SRHT	4.3 ± 0.3	24.4 ± 1.4	15.7 ± 0.6	8.7 ± 1.5
		SRHT + SB	5.3 ± 0.3	30.2 ± 2.3	18.2 ± 1.3	12.0 ± 1.1

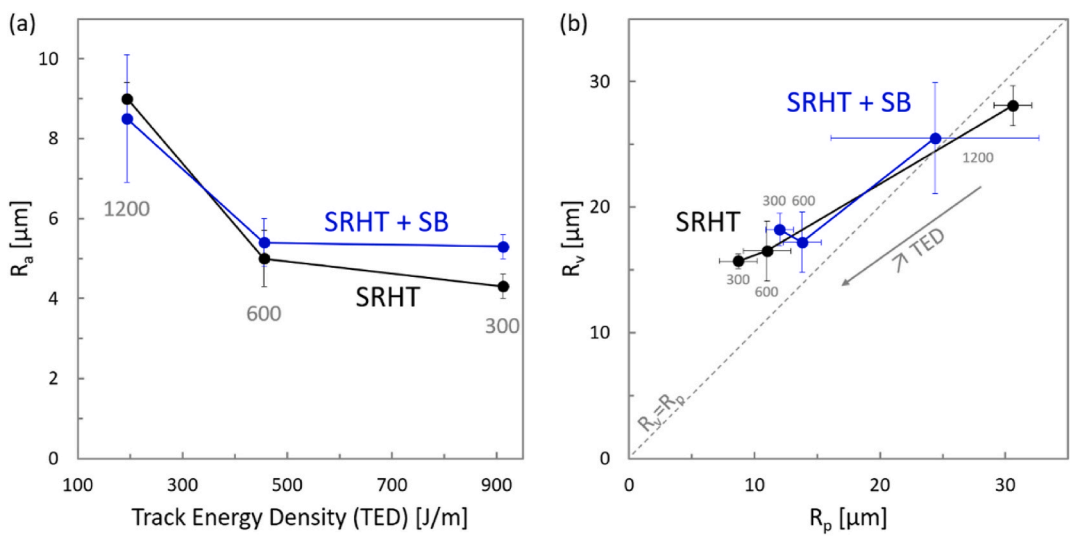

Fig. 2. (a) Evolution of the average roughness (R_a) with TED. (b) Comparison of valley (R_v) and peak (R_p) roughnesses. Contour scanning speeds are indicated for ease of understanding. Comparison between stress-relieved (SRHT) samples in black and stress-relieved + sandblasted (SRHT + SB) samples in blue. (For interpretation of the references to color in this figure legend, the reader is referred to the Web version of this article.)

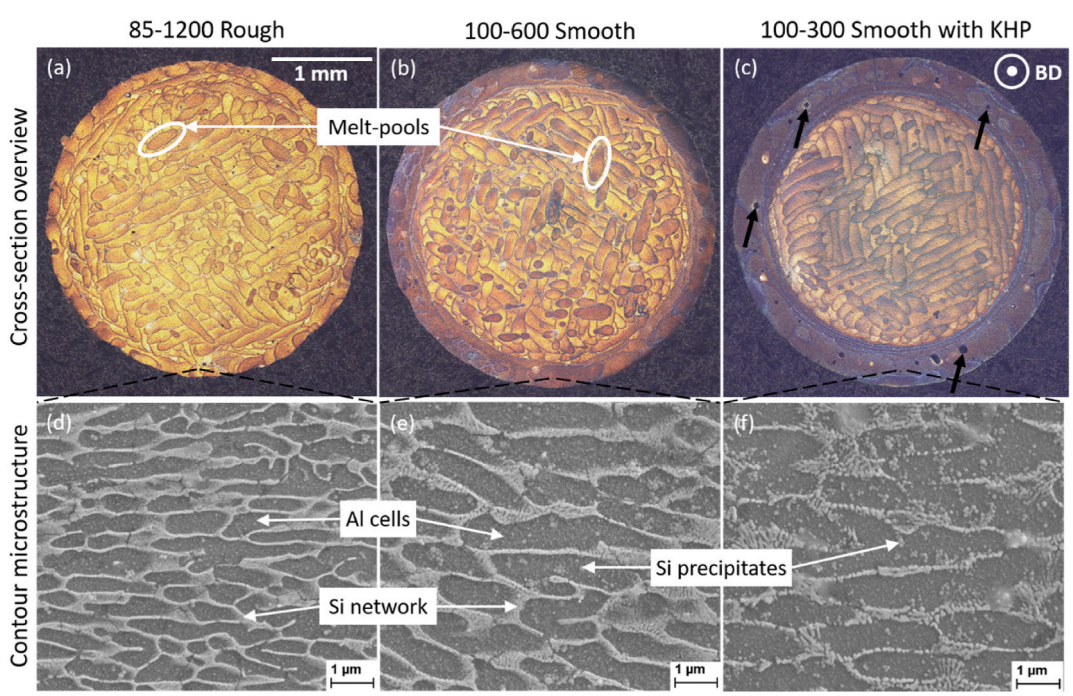

Fig. 3. (a–c) Optical micrographs of typical mesostructure of 85–1200 (low TED = 194 J/m), 100–600 (TED = 456 J/m), and 100–300 (high TED = 912 J/m) contoured samples in SRHT condition. (d–f) SEM micrographs of typical contour microstructure obtained with 85–1200, 100–600, and 100-300 L-PBF parameters after SRHT. Note that the bulk zones of the three categories of samples were manufactured with similar parameters (85–1200) and present microstructures similar to (d). The black arrows highlight some keyhole pores (KHP).

lower effect on the grooves present on the sample surface (known as a staircase effect) [16]. This explains why R_p decreases faster than R_v when the TED increases. The R_v and R_p values of the 85–1200 samples decrease by 9 % and 20 %, respectively, after sandblasting (top-right blue point in Fig. 2(b)). In contrast, the R_v and R_p values of the 100–600 and 100–300 samples increase after sandblasting, with a more pronounced rise observed for R_p. This indicates that sandblasting tends to create peaks rather than valleys on the surface. However, R_v still remains higher than R_p in all the SRHT + SB samples. After sandblasting, it is interesting to note that R_v remains the main contributor to R_z regardless of the TED, i.e. accounting for 51 %–60 % of R_z.

As indicated in the experimental procedure, an average roughness of 0.1 μm is obtained after extensive polishing. This value is significantly lower than those obtained for the sandblasted samples.

3.2. Mesostructures and microstructures

Fig. 3(a–c) presents typical mesostructures of the three families of contoured samples after stress-relief heat treatment (SRHT), from low (194 J/m) to high (912 J/m) contour TED. As expected, in 85–1200 contoured samples (Fig. 3(a)), bulk and contour zones have similar melt-pool widths (103.8 and 106.1 μm, respectively), as well as colors, reflecting similar microstructures. In 100–600 and 100–300 contoured samples (Fig. 3(b) and (c)), contour melt-pools are gradually larger (229.1 and 339.2 μm, respectively) and appear darker, reflecting coarser microstructures, due to the increased energy input. At higher magnification, Fig. 3(d–f) provides a comparison between the 85–1200, 100–600, and 100–300 SRHT microstructures from contour zones. It is worth noting that Fig. 3(d) is a representative microstructure of the bulk zone of all the samples, as well as of the contour zone of the 85–1200 family. It is possible to observe that the Si-network (lighter grey phase) around the Al cells (darker grey phase) in Fig. 3(d) remains interconnected, displaying little-to-no globularization. Likewise, it is possible to see that there are some Si precipitates inside the Al cell. In the 100–300 contour zone (Fig. 3(f)), the higher TED leads to a coarser Si-network around the Al cells, which has undergone a higher degree of globularization than in the core, leading to its degradation. Si precipitates inside the cells are also visible (lighter grey phase) and are coarser than in the bulk/85–1200 region (Fig. 3(d)). The contour microstructure in 100–600 samples (Fig. 3(e)) is intermediate between microstructures of 85–1200 and 100–300 zones (Fig. 3(d) and (f), respectively).

3.3. Porosity distribution

Porosity was characterized based on high-resolution CT scans (1000 slices, voxel size = 2 μm, hence 2 mm in thickness) of the three families of contoured samples after stress-relief heat treatment (SRHT). Porosity levels of 0.002 %, 0.007 %, and 0.035 % were obtained from low (194 J/m) to high (912 J/m) contour TED, respectively. Fig. 4(a–c) presents typical CT Z-projections, consisting in stacks of 200 slices centered on the minimal cross-section. As already visible in Figs. 3(c), 100–300 contour parameters generate numerous keyhole pores (KHP, white arrows) located in the central region of the contour melt pool. This is consistent with the higher TED used in the contour (912 J/m), which is associated with a keyhole melting mode and the appearance of such defects. KHP in the contour of 100–300 samples have a mean diameter of 73 ± 17 μm and are centered at a mean distance of 170 μm from the surface, right in the middle of the contour melt pool. Fig. 4(c) gives the impression of a "ring of pores", but it should be remembered that this is a stack of 200 slices. It is worth noting that, in a single cross-section, there are only a few keyhole pores (see Fig. 3(c)). The presence of KHP justifies the higher porosity level obtained for the 100–300 contoured sample (0.035 %). As highlighted by the white arrows in Fig. 4(b) and revealed by the intermediate level of porosity (0.007 %), keyhole pores are occasionally present in the contour of 100–600 contoured samples (only a few for the entire stack of 200 slices). In Fig. 4(a), the black arrow shows a lack-of-fusion defect present at the surface of the 85–1200 contoured sample.

In Fig. 5, CT data are presented with histograms in order to reflect the size distribution and the mean sphericity of the porosity, while discriminating between bulk and contour pores. Going from cold (85–1200, 194 J/m, Fig. 5(a)) to hot (100–300, 912 J/m, Fig. 5(c)) contour parameters clearly increases the porosity in the contour zone, while the volume of bulk porosity remains similar. For the 85–1200 et 100–600 contoured samples, Fig. 5(d) and (e) show that the smaller pores are rather spherical (equivalent diameter <30 μm, mean sphericity between 0.5 and 0.9), while a few bigger pores exist with a mean sphericity below 0.5. The first can be identified as metallurgical pores, while the latter can be related to lack-of-fusion defects in the 85–1200 sample or a mix between lack-of-fusion and keyhole defects in the 100–600 contoured sample, as it is operated at the onset of the keyholing mode. The histogram of the 100–300 contoured sample (Fig. 5(c)) reveals that two populations of pores clearly coexist, in addition to the metallurgical pores already observed in the 85–1200 and 100–600 samples. As demonstrated by Fig. 5(f), they are all rather spherical with a mean sphericity higher than 0.5 in any case. The population of bigger pores corresponds to the contour keyhole pores highlighted in Figs. 3(c) and 4(c). The secondary population of smaller pores, which are under 15 μm in size, may be associated to the "microporosities" observable near the outer and inner edges of the contour melt pool in Fig. 4(c). A few of these microporosities must also be present in the contour of 100–600 contoured sample, in the same vein as the few KHP, as shown by the presence of small contour pores in Fig. 5(b) (equivalent diameter

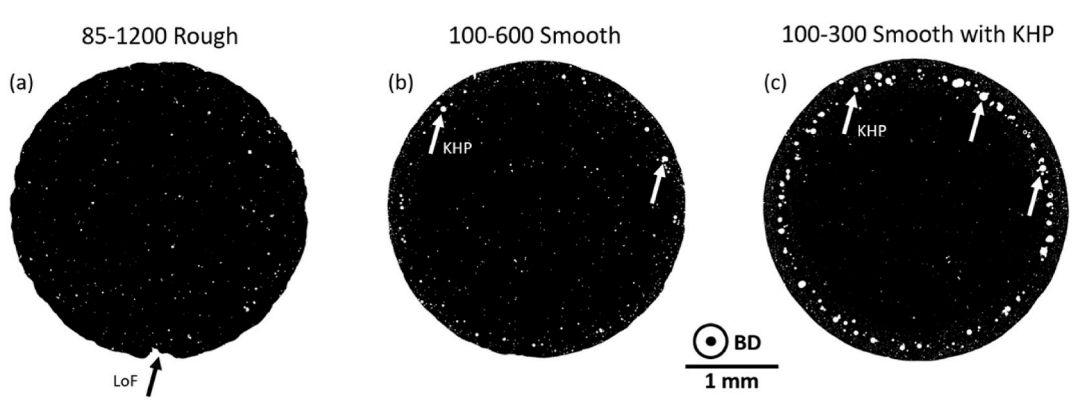

Fig. 4. Computed tomography (CT) Z-projections of (a) 85–1200 (low TED = 194 J/m), (b) 100–600 (TED = 456 J/m), and (c) 100–300 (high TED = 912 J/m) contoured samples in SRHT condition. Each projection is a stack of 200 slices with voxel size = 2 μm, hence representing 400 μm in thickness. The black arrow shows an open lack-of-fusion defect (LoF). The white arrows show keyhole pores (KHP).

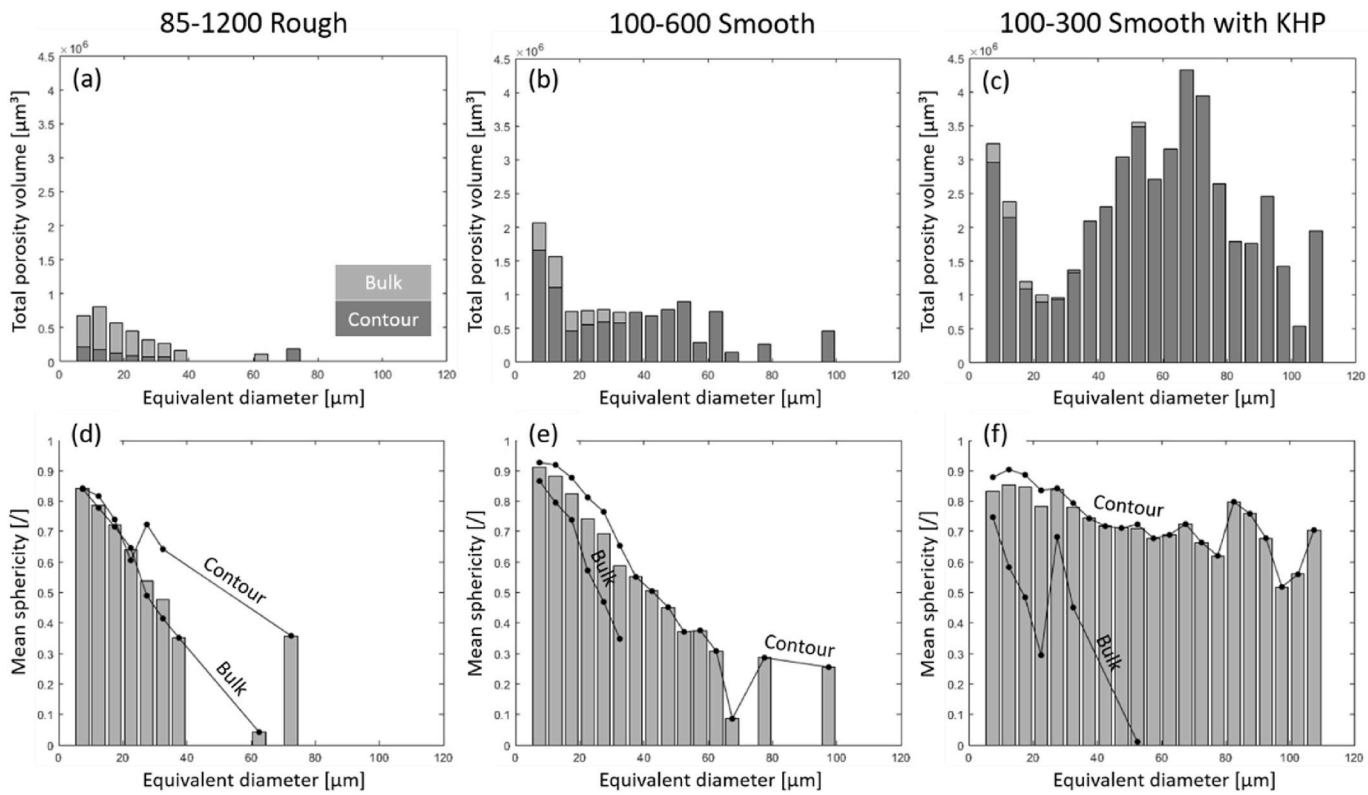

Fig. 5. (a–c) Histograms of bulk and contour porosity size distribution based on the full CT dataset (1000 slices, voxel size = 2 µm, 2 mm in thickness). (d–f) Corresponding mean sphericity of the pores for each bar of the histograms. The averages for bulk and contour are represented separately by the dots.

<15 µm) that are not present in the 85–1200 histogram. Table 5 summarizes the characterization of the porosity in the three families of samples.

Overall, no change in porosity distribution is expected after polishing and sandblasting, as these are surface post-processes. On average, sandblasting results in a change in sample diameter of less than 1 µm, while it decreases by around 100 µm after polishing, i.e. below the 170 µm corresponding to the average distance of the large keyhole pores from the surface.

3.4. Static properties

The average values for the yield strength, ultimate tensile strength (UTS) and elongation at break are summarized in Table 6. In all cases, the differences in mechanical properties among sample families are not beyond the margins of error, which indicates that the static properties are not significantly affected by the contour parameters. Zhao et al. identified the globularization of the Si network as the major contributing factor that decreases the strength of AlSi10Mg and imparts ductility [39]. The fact that there is no evidence of significant globularization in the bulk of the samples (as shown in Fig. 3(d)), which encompasses the main load-bearing region, is consistent with the relatively low ductility of the alloy.

Table 5
Analysis of the porosity in the three families of samples. LoF = lack-of-fusion defects, KHP = keyhole pores.

	Bulk	Contour
85–1200 Rough	Metallurgical pores A few LoF	Metallurgical pores A few LoF
100–600 Smooth		A few microporosities Metallurgical pores A few LoF and a few KHP
100–300 Smooth with KHP		Microporosities Metallurgical pores "Ring" of KHP

Table 6
Static properties of the three families of samples in stress-relieved condition (SRHT).

	Yield Strength, 0.2 % [MPa]	Ultimate Tensile Strength [MPa]	Elongation at break [/]
85–1200 Rough	238.9 ± 1.7	403.8 ± 3.7	0.04 ± 0.0015
100–600 Smooth	244.4 ± 9.0	413.0 ± 6.7	0.04 ± 0.0003
100–300 Smooth with KHP	239.0 ± 6.1	391.9 ± 0.1	0.03 ± 0.0010

3.5. Fatigue performance of SRHT samples

Fig. 6 presents the results of the fatigue tests carried out on the stress-relieved (SRHT) samples with as-built surface condition, as standard Wöhler curves. The smooth samples contoured by both the 100–600 and 100–300 parameter sets present a better fatigue resistance than the reference 85–1200 rough samples. Kohout-Věchet fitting curve [38], described in Equation (1), has been plotted for each family of samples. The improvement in fatigue resistance for the 100–300 samples is higher than for the 100–600 samples and seems uniform across all the stress levels. In contrast, the trendline of the 100–600 samples presents a steeper decline. Note that none of the samples reaches 10^7 cycles in the tested stress range. It is therefore not possible to determine a technical fatigue strength, via the run-outs, for the SRHT samples. This is in line with Aboulkhair et al. having technical fatigue strengths below the tested stress range for similar material and close conditions (around 63 MPa and 99 MPa for as-built and heat-treated conditions, respectively) [25].

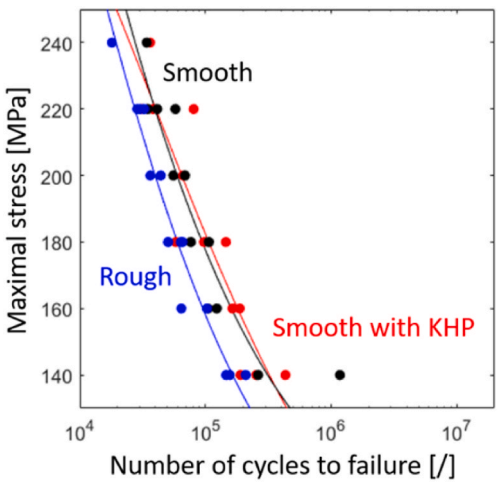

Fig. 6. Wöhler curves for the SRHT samples: 85–1200 rough (blue), 100–600 smooth (black), and, 100–300 smooth with KHP (red) with as-built surface condition. Experimental data points are fitted with Kohout-Vĕchet model [38], see Equation (1). (For interpretation of the references to color in this figure legend, the reader is referred to the Web version of this article.)

Table 7 provides a summary of the identified fatigue initiating sites. In greater detail, Table S1 in Supplementary Materials provides the initiating sites as a function of the stress levels. In SRHT condition, fatigue failure of almost all the samples (36 out of 42) started from the surface, whatever the contour parameters. The defects that initiate fatigue failure from the surface are difficult to identify (as illustrated in Fig. 7), but are most likely surface irregularities, notches or oxides. More specifically, in the 85–1200 contoured samples, lack-of-fusion (LoF) defects at or close to the surface were initiating fatigue cracks in 4 cases out of 14 (see Table 7 and an example in Fig. 8(a)). Multiple initiation sites are visible on the fracture surface of 18 samples (out of 42), especially in 85–1200 rough samples because of a higher proportion of surface defects (in 9 samples out of 14 in that case). Fig. 9 illustrates an extreme example with about ten initiation sites visible on the fracture surface. Directly related to this, the initiating crack zone of the 85–1200 sample in Fig. 7(a) has a larger number of ratcheting marks, indicating the presence of more microcracks generated from the rougher surface. It is worth noting that subsurface keyhole pores (KHP) seem to play no role in fatigue initiation in 100–300 samples (see Fig. 7(c)). In one case out of 14 (see Fig. 8(b)), a spherical subsurface pore adjacent another surface defect was responsible for initiation, but it is not identified as a keyhole defect, as it does not appear to be located in the center line of the contour melt pools.

3.6. Fatigue performance of polished and sandblasted SRHT samples

In order to evaluate the decoupled effect of contour keyhole porosity and improved surface quality, the stress-relieved samples were compared with homologous polished (SRHT + P) and sandblasted (SRHT + SB) samples. The reference 85–1200 samples (initially rough) present a small improvement after polishing and a slightly higher increase after sandblasting (see Fig. 10). Both post-processes are known from literature to improve fatigue life: polishing by reducing surface roughness [40] and sandblasting by inducing compressive residual stress at the surface [37]. After polishing and sandblasting, half of the 85–1200 broken samples (11 out of 20) initiated on LoF defects at or

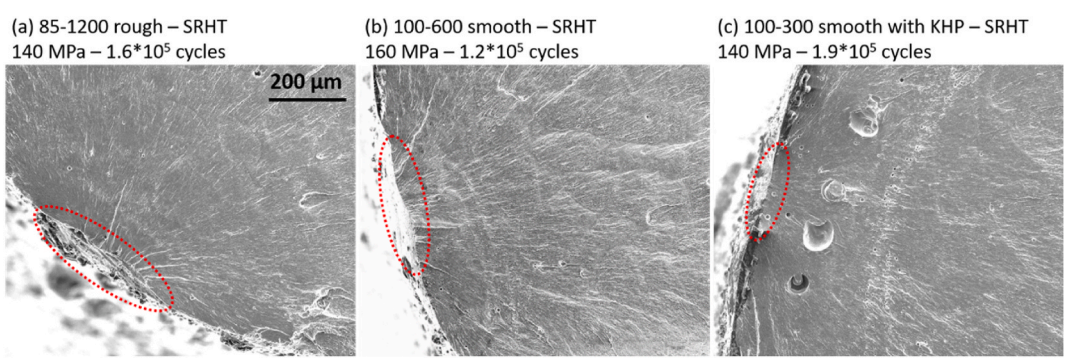

Fig. 7. SEM micrographs of fatigue fracture surface of SRHT (a) 85–1200 rough, (b) 100–600 smooth, and (c) 100–300 smooth with KHP samples with as-built surface condition. Red dotted circles highlight the areas of the surface from which the fatigue initiated, without a specific defect being identified. (For interpretation of the references to color in this figure legend, the reader is referred to the Web version of this article.)

Table 7
Identification of fatigue failure initiating sites for all the tested samples. The ratio in brackets indicates the occurrence among all the tested samples. SRHT = stress-relieved, P = polished, SB = sandblasted conditions, KHP = keyhole pores, LoF = lack-of-fusion defects.

	SRHT	SRHT + P	SRHT + SB
85–1200 (Initially) Rough	Surface (10/14) LoF at/close to surf (4/14)	LoF at/close to surf (7/12) Surface (5/12)	LoF at/close to surf (4/12) Run-outs (4/12) Surface (4/12)
100–600 (Initially) Smooth	Surface (13/14) Subsurf defect (1/14)	Subsurf defect (5/13) Surface (4/13) Run-outs (3/13) Subsurf KHP (1/13)	Surface (9/16) Run-outs (4/16) Undefined (2/16) LoF in bulk/between bulk and contour (1/16)
100–300 (Initially) Smooth with KHP	Surface (13/14) Subsurf defect (1/14)	Surface (6/12) Opened subsurf KHP (5/12) Subsurf KHP (1/12)	Surface (6/15) LoF in bulk/between bulk and contour (3/15) KHP in contour (3/15) Run-outs (3/15)

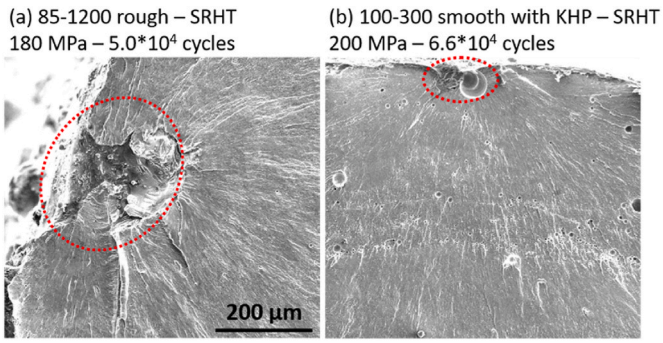

Fig. 8. SEM micrographs of fatigue fracture surface of SRHT samples with as-built surface condition. Red dotted circles highlight (a) a lack-of-fusion initiating defect in a 85–1200 rough sample, and (b) a subsurface spherical pore combined with a surface irregularity that initiated fracture in a 100–300 sample (smooth with KHP). (For interpretation of the references to color in this figure legend, the reader is referred to the Web version of this article.)

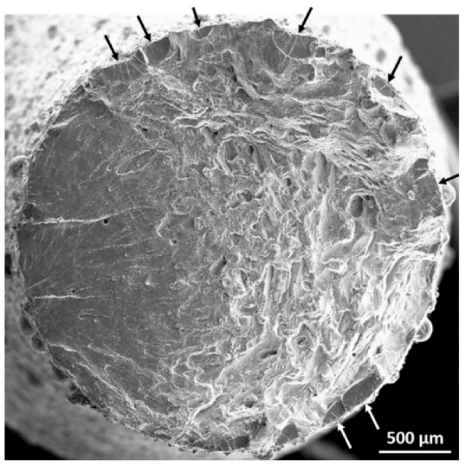

Fig. 9. SEM micrograph of the fatigue fracture surface of a SRHT 85–1200 rough sample (200 MPa–4.4*10^4 cycles) presenting multiple initiation sites, highlighted by black or white arrows.

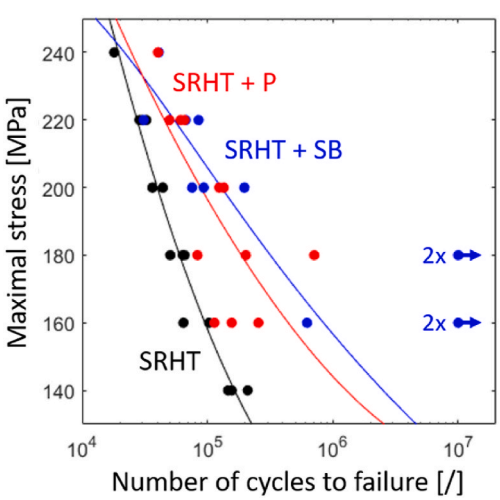

Fig. 10. Wöhler curves for the reference 85–1200 samples (initially rough) in SRHT (black), polished (red), and sandblasted (blue) conditions. Experimental data points are fitted with Kohout-Věchet model [38], see Equation (1). Arrowed points represent run-outs. "2x" means that 2 samples were tested and ran out at these stress levels. (For interpretation of the references to color in this figure legend, the reader is referred to the Web version of this article.)

close to the surface (similarly to Fig. 8(a)), while in the others (9 out of 20) no LoF defect could clearly be identified (see Table 7, as well as Table S2 and Table S3 in Supplementary Materials). Four sandblasted samples reached 10^7 cycles, at maximal stress levels of 160 and 180 MPa, placing their technical fatigue strength in this interval.

Fig. 11 presents the results for the 100–600 contoured samples (initially smooth). It shows that both polishing and sandblasting have a significant positive effect on fatigue life. SRHT + P and SRHT + SB 100–600 samples perform much better than SRHT samples without surface treatment, particularly at lower stress levels. **By combining 100–600 contour parameters and polishing or sandblasting, the fatigue lifetime of heat-treated samples is increased by two orders of magnitude at lower stress levels (160–180 MPa).** Three polished and four sandblasted samples reached 10^7 cycles, at maximal stress levels of 160 and 180 MPa. Both surface post-processes therefore provide similar technical fatigue strength and close fit curves in the tested stress range.

Fatigue cracks initiated on (sub)surface irregularities, notches or oxides in most of the 100–600 SRHT + P and SRHT + SB samples (18 cases out of 20, see Table 7, as well as Table S2 and Table S3 in Supplementary Materials). Fig. 12 illustrates two exceptions: (a) in a polished sample, a subsurface KHP initiated fracture, and (b) in a sandblasted sample, fracture was initiated on a LoF defect located in the bulk or at the boundary between bulk and contour.

Fig. 13 presents the Wöhler curves of the 100–300 contoured samples (initially smooth with KHP). On the one hand, polished samples perform reasonably better than SRHT ones. On the other hand, sandblasting has a significantly positive impact on the fatigue life, with an improvement close to two orders of magnitude at 160–180 MPa. Except at the higher stress level (220–240 MPa), the lifetime of 100–300 polished samples lies between SRHT and SRHT + SB samples. Three run-outs occurred for maximal stress of 160 and 180 MPa, giving again a technical fatigue strength in this range for 100–300 SRHT + SB samples.

In 100–300 polished samples, surface initiation occurred for half of the cases (6 out of 12). Fracture initiated on (opened) subsurface KHP in the six other cases, as illustrated in Fig. 14(a). The type of initiating defect is more dispersed in the case of 100–300 sandblasted samples (see Table 7, as well as Table S2 and Table S3 in Supplementary Materials): surface defects (6 out of 15), LoF defects located in the bulk or at the

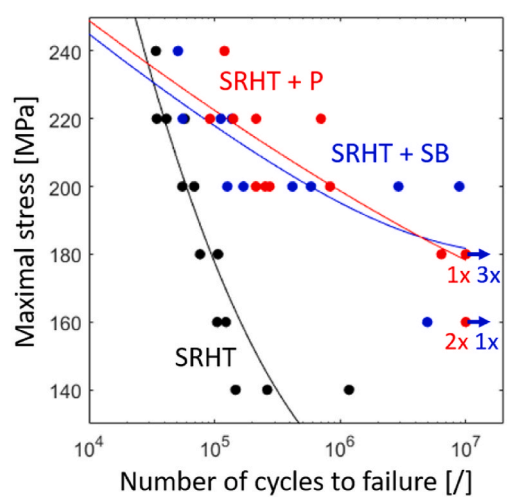

Fig. 11. Wöhler curves for the 100–600 samples (initially smooth) in SRHT (black), polished (red), and sandblasted (blue) conditions. Experimental data points are fitted with Kohout-Věchet model [38], see Equation (1). Arrowed points represent run-outs. Both polished and sandblasted samples ran out at 160 and 180 MPa "1, 2, or 3x" means that 1, 2, or 3 samples were tested and ran out at these stress levels. (For interpretation of the references to color in this figure legend, the reader is referred to the Web version of this article.)

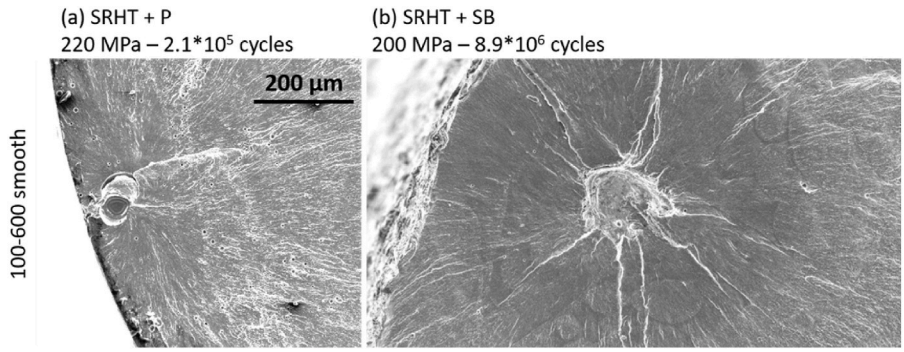

Fig. 12. SEM micrographs highlighting exceptional initiating defects in 100–600 samples (initially smooth): (a) a subsurface keyhole pore in SRHT + P condition, and (b) a lack-of-fusion defect close to the bulk/contour boundary in SRHT + SB condition.

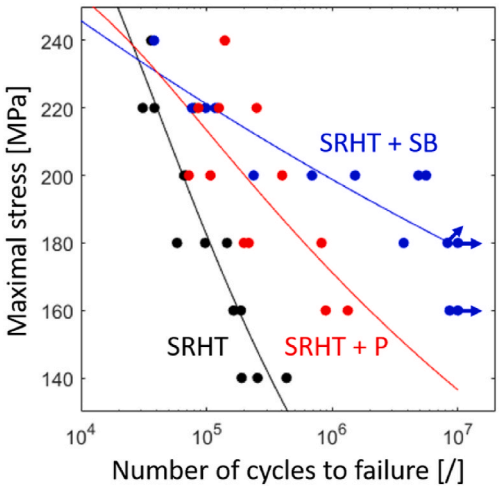

Fig. 13. Wöhler curves for the 100–300 samples (initially smooth with KHP) in SRHT (black), polished (red), and sandblasted (blue) conditions. Experimental data points are fitted with Kohout-Věchet model [38], see Equation (1). Arrowed points represent run-outs. (For interpretation of the references to color in this figure legend, the reader is referred to the Web version of this article.)

boundary between contour and bulk (3 out of 15, Fig. 14(b)), and KHP in the contour (3 out of 15, Fig. 14(c)) were identified. It is worth noting that, after polishing, initiating KHP were opened on the surface (Fig. 14 (a)), while they were still closed after sandblasting (Fig. 14(c)).

4. Discussion

4.1. Effect of roughness and porosity on fatigue properties of SRHT samples

The fatigue performance of net-shaped vertically-built stress-relieved AlSi10Mg fatigue samples reveals that the increased contour TED in the 100–600 and 100–300 smooth samples results in a better fatigue life than the reference 85–1200 rough contoured samples (see Fig. 6). The 100–600 and 100–300 samples present a lower surface roughness than the 85–1200 samples (see Table 4), while only the 100–300 samples present a significant amount of subsurface keyhole pores along the contour (see Fig. 4 and Table 5). This indicates that roughness rather than porosity is the controlling factor for fatigue performance of samples with as-built surface condition in the present study.

Moreover, the keyhole porosity (with the larger KH pores located at a mean distance of 170 µm from the surface) does not represent a detrimental factor for fatigue performance, since the SRHT 100–300 samples presented the best overall fatigue life, as demonstrated by Fig. 6. Fig. 7 (c) reinforces this hypothesis, as one can see that initiation takes place at the surface, independently of the presence of subsurface KHP. Piette et al. came to the same conclusion [36]: their "healing" contour (second contour pass with a lower TED) does not improve the fatigue properties, although it reduces the quantity and size of the contour pores, while not affecting the roughness too much. These recent results (present study and [36]) contradict the conclusion of Raja's review published in 2022 [33], which concluded that pores are the principal defects initiating cracks in AlSi10Mg manufactured by L-PBF.

Table 8 compares the values of the Kohout-Věchet fitting parameters, see Equation (1), for the stress-relieved samples in as-built surface condition (SRHT in shaded lines). The fitting parameter b could be related to the fatigue strength exponent, representing the Wöhler curve's slope on a log-log scale in the linear regime (approximative

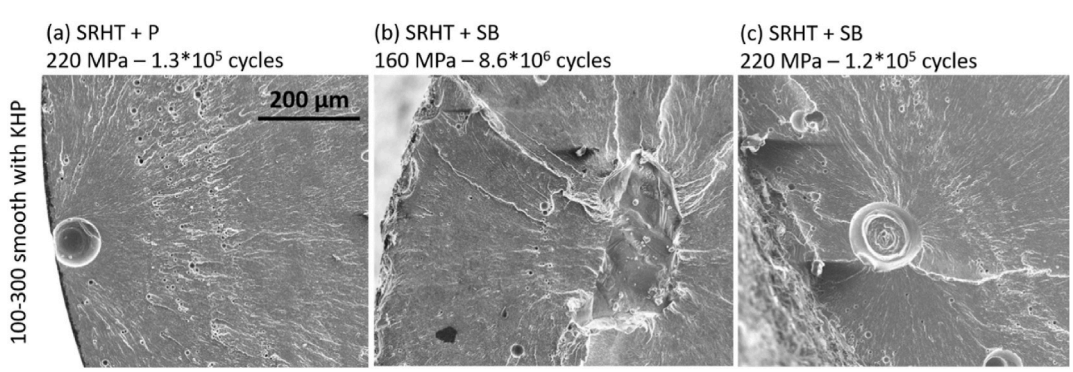

Fig. 14. SEM micrographs highlighting initiating defects in 100–300 samples (initially smooth with KHP): (a) an opened subsurface keyhole pore in SRHT + P condition, (b) a lack-of-fusion defect close to the contour/bulk boundary in SRHT + SB condition, and (c) a keyhole pore in the contour in SRHT + SB condition.

Table 8
Contour TED, average arithmetic roughness (R_a), and Kohout-Věchet fitting parameters, see Equation (1), for 85–1200 (initially) rough, 100–600 (initially) smooth, and 100–300 (initially) smooth with KHP samples. Comparison between stress-relieved (SRHT), stress-relieved + polished (SRHT + P), and stress-relieved + sandblasted (SRHT + SB) conditions.

	Contour TED [J/m]	Post-processing	R_a [μm]	*a* [MPa]	*b* [/]	*B* [/]	*C* [/]
85–1200 (Initially) Rough	194	SRHT	9.0	3513	−0.28	1.9e3	1e6
		SRHT + P	~0.1	936	−0.15	1e2	5e6
		SRHT + SB	8.5	776	−0.12	1e4	3.7e8
100–600 (Initially) Smooth	456	SRHT	5.0	2696	−0.25	1e2	1e6
		SRHT + P	~0.1	353	−0.05	2.4e2	8.3e7
		SRHT + SB	5.4	354	−0.05	1e2	5e6
100–300 (Initially) Smooth with KHP	912	SRHT	4.3	2631	−0.24	9.8e3	1e9
		SRHT + P	~0.1	608	−0.10	9.8e3	1e9
		SRHT + SB	5.3	339	−0.05	1e2	9.3e8

range from 10^3 to 10^6 cycles). It is related to the material's sensitivity to cyclic loading: a smaller absolute value of *b* (i.e. higher value as *b* is negative) implies a greater increase in fatigue life for a given decrease in stress range. On the other hand, the fitting parameter *a* can be associated to the fatigue strength coefficient and represents the intersection with the stress range axis. However, the value of *a* is difficult to compare from one curve to another because it is highly dependent on the value of *b*. Typically, curves with a steep slope (larger absolute value of *b*) will reach higher intercept values although performing less well at a higher number of cycles. According to the definition of Kohout and Věchet [38], *B* and *C* represent the numbers of cycles from which the fatigue curve bends (onset and end of the linear regime with slope *b*, respectively). The values of *b* will be at the heart of the discussion, while *a*, *B*, and *C* are given for information only.

In the absence of surface post-process, all sample families present close *b* parameters (−0.24 to −0.28), hence material sensitivities to fatigue. The 85–1200 samples have the highest *a* value balanced by a slightly larger absolute value of *b* (steeper slope), while the fatigue strength coefficient *a* of 100–600 and 100–300 samples are close. Comparison with the literature is difficult because of the large ranges of parameters in the manufacturing, post-processing and testing conditions. Only Aboulkhair et al. [25] provide results close to the present set of samples without surface post-process: $a = 832$ and 501 MPa and $b = -0.22$ and −0.15 for as-built and heat-treated conditions, respectively. Despite a much higher roughness (17.1 μm), they have a lower sensibility to cyclic loading, but at the expense of the fatigue strength coefficient, which is far lower than present values. This difference may be attributed to the pre-heating of their building plate to 180 °C, as well as to the hotter temperature of their heat-treatment (solution heat-treatment for 1h at 520 °C followed by artificial ageing for 6h at 160 °C), leading to a possible softening of the material. Indeed, after the two-step heat-treatment, they observed grain growth and a totally globularized Si network [25], which is not the case here (see Fig. 3).

4.2. Effect of surface post-processing on fatigue properties

The aim of this section is to assess (1) the extent to which fatigue life could be improved by surface post-processing and (2) the independent effect of keyhole pores in the 100–300 samples compared to the 100–600 (without keyhole porosity or, more precisely, with considerably less KHP). For this purpose, Table 8 summarizes Kohout-Věchet fitting parameters, together with the contour TED and the average roughness, also for polished and sandblasted conditions.

4.2.1. Effect of polishing

Polishing the samples improves the overall surface condition, as any attached unmelted powder particles are removed, and the grooves on the surface are similarly extinguished. Whatever the contour parameters, polishing has a positive impact on the fatigue life, by shifting the Wöhler curves to higher stress-longer lifetime (see Figs. 10, 11 and 13). The sensibility to cyclic loading is significantly decreased in any cases, as demonstrated by lower absolute values of *b* in Table 8 (−0.05 to −0.15) in comparison to as-built surface condition (−0.24 to −0.28).

Fig. S4 compares the Wöhler curves of all polished samples. It is worth noting that the performances of the SRHT + P 100–600 (initially smooth) samples are better than that of the SRHT + P 100–300 (initially smooth with KHP) samples, unlike the SRHT case (see Fig. 6). This is also demonstrated by the smaller absolute value of *b* in Table 8: −0.05 and −0.10 for the SRHT + P 100–600 and 100–300 samples, respectively. The performances of the 85–1200 initially rough polished samples remain the lowest among the tested samples.

The reason behind this difference in polishing "efficiency" on fatigue life between 100-600 and 100–300 samples is the effect of the opened porosity on the polished surface of 100–300 contoured samples, as illustrated in Fig. 15. The polishing procedure removes approximately 100 μm in diameter and improves greatly the roughness. However, it can lead to the opening and exposure at the surface of defects or pores, particularly KHP or microporosities widely present in the contour of 100–300 samples (see Fig. 4(c) and Table 5) or LoF defects in 85–1200 samples (see Fig. 4(a)). This does not happen in the case of 100–600 samples because, by operating at the onset of the keyholing mode, there are less likely keyhole pores, microporosities, or LoF defects in the contour zone (see Fig. 4(b)), hence on the polished surface, as evidenced in Fig. 15(a).

In the 100–300 samples, while KHP should not be opened by the polishing procedure based on average values (KHP mean diameter of 73 μm, located at 170 μm, removal of 50 μm), this can statistically occur when a KHP is located closer to the surface. In 6 cases out of 12 (see Table 7), large keyhole pores (between 70.0 and 145.3 μm in diameter) were identified as responsible for crack initiation (as shown in Fig. 14 (a)). In addition to KHP, microporosities can also create hotspots for

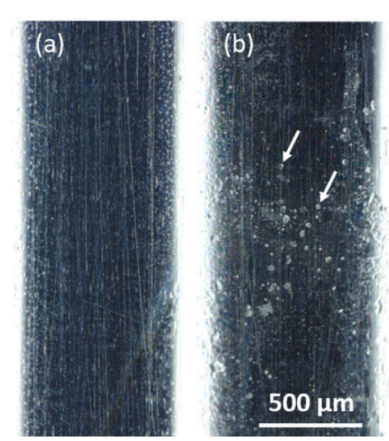

Fig. 15. Comparison of the polished surface of typical a) 100–600 (initially smooth) and b)100–300 (initially smooth with KHP) samples.

crack nucleation, as highlighted by the white arrows in Fig. 15(b). However, the direct link with the initiating defect on the fracture surfaces cannot be established with certainty in these cases (referred to as surface initiation in Table 7). In the 85–1200 initially rough family, lack-of-fusion close to or at the surface were identified as initiating defects in most of the polished samples (7 out of 12).

A first comparison with literature is possible with the results of Hamidi Nasab et al. [40]. They obtained an interestingly low sensibility to cyclic loading on machined and polished samples ($b = -0.05$, close to the 100–600 SRHT + P samples), but with a lower fatigue strength coefficient ($a = 174$ MPa). On their side, Santos et al. [23] obtained $a = 840$ MPa and $b = -0.12$ on stress-relieved and polished samples, in between the 85–1200 and 100–300 SRHT + P results, putting these two categories of samples "within the standards of literature". On the other hand, the 100–600 SRHT + P family exhibits excellent performances, with a very low absolute value of the fatigue strength exponent ($b = -0.05$) rarely reported in literature. One example and a basis of comparison is provided by Santos et al. with similar performances ($a = 411$ MPa, $b = -0.04$) obtained after friction stir processing and polishing [23]. Friction stir processing drastically reduces porosity and eliminates totally the larger pores, but this is achieved by adding an additional post-processing step [23]. This last comparison highlights the very interesting efficiency of the present contour-optimized parameters (at the onset of keyholing) in order to avoid any defect or porosity in the contour region, which is the most critical one for fatigue properties, while avoiding the use of post-processing.

4.2.2. Effect of sandblasting

Stress-relieved + sandblasted samples present the overall best performances, although similar to the polished condition in the 100–600 initially smooth samples (see Figs. 10, 11 and 13). This is reflected by a lower sensibility to cyclic loading, with the smallest absolute values of b in Kohout-Věchet fits (−0.05 to −0.12 in Table 8) in comparison to SRHT samples (−0.24 to −0.28). In addition, Fig. S5 shows that 100–300 and 100–600 initially smooth samples (with and without KHP) present comparable results and very close fit curves after sandblasting.

In the literature, it is known that sandblasting may reduce roughness and induces compressive residual stresses by localized plastic deformation of the surface, which improve fatigue life [19,20]. Fig. 16 presents the evolution of the average surface roughness in SRHT and SRHT + SB samples compared to the improvement reported by Avanzini et al. [19]. The latter obtained a reduction in roughness of almost a factor of 2 after sandblasting, which was attributed to the elimination of surface irregularities (satellites, balling, stuck particles) [19]. However, when contour-optimized parameters are used, sandblasting no longer improves surface quality and may even lead to a slight increase in surface roughness (+0.4 and + 1 μm for 100–600 and 100–300 contoured samples, respectively). This is attributed to the low roughness level achieved in the present work by optimizing the contour parameters (R_a = 4.3–5 μm), which is already 2–3 times lower than that of the AB samples reported in the literature [19,25,40].

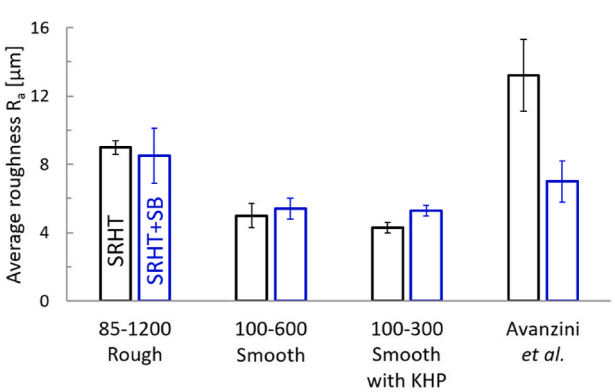

Fig. 16. Evolution of R_a after sandblasting in SRHT 85–1200 (rough), 100–600 (smooth) and 100–300 (smooth with KHP) samples, and comparison with the literature [19].

In the absence of any significant improvement in surface roughness, the improvement in fatigue life is attributed to compressive residual stresses. Bagherifad et al. [32] reported that by sandblasting AlSi10Mg samples, it was possible to switch from tensile to compressive residual stress at the surface of the sample (i.e. switch from 70 MPa to −90 MPa). They even reached a peak compressive stress of −145 MPa at a depth of 0.12 mm. These results have been reproduced by Avanzini et al. [19], reporting residual stress switching from 76 MPa to −105 MPa after sandblasting. They obtained a fatigue strength exponent ($b = -0.13$) comparable to the 85–1200 SRHT + SB family, but with a lower fatigue strength coefficient ($a = 309$ MPa) [19]. On their side, Hamidi Nasab et al. reported a and b values of 174 MPa and −0.06 and [40], closer to the optimized 100–600 and 100–300 contoured families. They did not measure directly the residual stress, but used literature to claim that compressive residual stresses are generated during sandblasting [41, 42].

4.2.3. Comparison between polishing and sandblasting

Polishing and sandblasting provide similar results on 100–600 contoured samples (initially smooth), hence with low as-built roughness and in the absence of KHP, as evidenced in Fig. 11. Table 8 shows that the Kohout-Věchet fitting parameters are very close ($a = 353$ or 354 MPa and $b = -0.05$), although the two families of samples have very different roughnesses (~0.1 vs 5.4 μm, respectively). It means that a well-polished surface provides similar fatigue life than surface compressive residual stresses. HamidiNasab et al. reached a similar conclusion. They compared machined and polished samples with sandblasted samples, and the two categories showed very similar fatigue behaviors despite different roughnesses [40].

In 100–300 samples (initially smooth with KHP), the presence of large KHP and microporosities in the contour zone leads to earlier fracture after polishing, while sandblasting offers better fatigue life. It is reflected in the values of Kohout-Věchet fitting parameters: 608 MPa and −0.1 vs 339 MPa and −0.05 for polished and sandblasted samples, respectively.

It is worth noting that SRHT + P 100–600, SRHT + SB 100–600, and SRHT + SB 100–300 samples present similar fatigue performances, despite different roughnesses and the absence/presence of KHP. In addition to similar Kohout-Věchet fitting parameters, these three families of samples also present comparative technical fatigue strength in the 160–180 MPa interval. From a practical point of view, it should be noted that mirror polishing is time-consuming and cannot be easily applied to complex parts or structures. Sandblasting, on the other hand, is much faster and can be applied to more complex shapes, at a much larger scale and can be easily automated.

5. Conclusions

This study investigated the influence of roughness and subsurface porosity on the fatigue behavior of net-shaped, vertically built AlSi10Mg L-PBF samples. By tailoring contour parameters, three families of samples were produced: (i) with a rough surface, (ii) with a smooth surface, and (iii) with a smooth surface and subsurface keyhole pores. Each set was evaluated in stress-relieved state with different surface conditions: as-built, mirror-polished, and sandblasted. The following conclusions can be drawn:

- Optimized contour parameters at the onset of keyholing or in keyhole mode (TED = 456 or 912 J/m) provide a low lateral surface roughness. Fatigue performances in as-built surface condition are improved but remain low without surface post-processing.

- When optimized contour parameters are applied, roughness cannot be further improved with sandblasting. Despite higher roughness, stress-relieved + sandblasted samples have a better fatigue life than stress-relieved equivalent parts.
- Lack-of-fusion defects are highly detrimental for fatigue, especially when appearing near the surface. Avoiding (sub)surface LoF defect by means of "high TED" contour parameters improves fatigue properties in any surface condition. Indeed, in comparison to the 85–1200 case (TED = 194 J/m), the optimized contour parameters provide a better fatigue life, whether or not surface post-processing is applied.
- The "ring" of keyhole pores in the contour is not detrimental for fatigue, except when polishing is applied due to the "opening" of some (micro)pores. It is thus acceptable to use contour parameters with a high TED (e.g. 912 J/m) that favor low roughness, even if this means forming subsurface keyhole pores.
- Contour parameters in keyhole mode are a good compromise if high fatigue performances are needed in as-built and sandblasted conditions (e.g. parts with complex shapes or internal channels where sandblasting cannot be applied everywhere). Contour parameters at the onset of keyholing (e.g. TED = 456 J/m) should be preferred if the application requires to avoid any risk of porosity.

CRediT authorship contribution statement

Camille van der Rest: Writing – review & editing, Writing – original draft, Visualization, Methodology, Investigation, Formal analysis, Data curation, Conceptualization. **Rodrigo Arturo Manzano Navarrete:** Writing – original draft, Investigation. **Aude Simar:** Writing – review & editing, Supervision, Resources, Funding acquisition. **Olivier Poncelet:** Writing – review & editing, Supervision, Investigation, Funding acquisition, Conceptualization.

Declaration of competing interest

The authors declare that they have no known competing financial interests or personal relationships that could have appeared to influence the work reported in this paper.

Acknowledgements and funding sources

The authors would like to thank Dr. Grzegorz Pyka for his help with the X-Ray tomography measurements. The authors acknowledge the financial support from the Wallinov LongLifeAM project (convention n∘1810016) funded by the Service public de Wallonie, Economie Emploi Recherche (SPW-EER), Belgium. This work was also supported by the Walloon Region through the WINGS (Walloon Innovation for Green Skies) project (RW 8441). This research was also supported by the Fonds de la Recherche Scientifique – FNRS - PDR -T.0209.23.

Appendix A. Supplementary data

Supplementary data to this article can be found online at https://doi.org/10.1016/j.msea.2025.148885.

Data availability

Data will be made available on request.

References

[1] S.A. Tofail, E.P. Koumoulos, A. Bandyopadhyay, S. Bose, L. O'Donoghue, C. Charitidis, Additive manufacturing: scientific and technological challenges, market uptake and opportunities, Mater. Today 21 (1) (2018) 22–37, https://doi.org/10.1016/j.mattod.2017.07.001.
[2] L. Zhao, L. Song, J.G.S. Macías, Y. Zhu, M. Huang, A. Simar, Z. Li, Review on the correlation between microstructure and mechanical performance for laser powder bed fusion AlSi10Mg, Addit. Manuf. 56 (2022) 102914, https://doi.org/10.1016/j.addma.2022.102914.
[3] S. Lathabai, Additive manufacturing of aluminium-based alloys and composites, Fundamental Alumini. Metallur. (2018) 47–92, https://doi.org/10.1016/B978-0-08-102063-0.00002-3.
[4] A. Aversa, G. Marchese, A. Saboori, E. Bassini, D. Manfredi, S. Biamino, M. Lombardi, New aluminum alloys specifically designed for laser powder bed fusion: a review, Materials 12 (7) (2019) 1007, https://doi.org/10.3390/ma12071007.
[5] X. Liu, C. Zhao, X. Zhou, Z. Shen, W. Liu, Microstructure of selective laser melted AlSi10Mg alloy, Mater. Des. 168 (2019) 107677, https://doi.org/10.1016/j.matdes.2019.107677.
[6] K. Kempen, L. Thijs, J. Van Humbeeck, J.P. Kruth, Mechanical properties of AlSi10Mg produced by selective laser melting, Phys. Procedia 39 (2012) 439–446, https://doi.org/10.1016/j.phpro.2012.10.059.
[7] T.M. Mower, M.J. Long, Mechanical behavior of additive manufactured, powder-bed laser-fused materials, Mater. Sci. Eng. 651 (2016) 198–213, https://doi.org/10.1016/j.msea.2015.10.068.
[8] E. Brandl, U. Heckenberger, V. Holzinger, D. Buchbinder, Additive manufactured AlSi10Mg samples using Selective Laser Melting (SLM): microstructure, high cycle fatigue, and fracture behavior, Mater. Des. 34 (2012) 159–169, https://doi.org/10.1016/j.matdes.2011.07.067.
[9] S. Patel, M. Vlasea, Melting modes in laser powder bed fusion, Materialia 9 (2020) 100591, https://doi.org/10.1016/j.mtla.2020.100591.
[10] W.H. Kan, L.N.S. Chiu, C.V.S. Lim, Y. Zhu, Y. Tian, D. Jiang, A. Huang, A critical review on the effects of process-induced porosity on the mechanical properties of alloys fabricated by laser powder bed fusion, J. Mater. Sci. 57 (21) (2022) 9818–9865, https://doi.org/10.1007/s10853-022-06990-7.
[11] R. Snell, S. Tammas-Williams, L. Chechik, A. Lyle, E. Hernández-Nava, C. Boig, I. Todd, Methods for rapid pore classification in metal additive manufacturing, Jom 72 (2020) 101–109, https://doi.org/10.1007/s11837-019-03761-9.
[12] J. Metelkova, L. Vanmunster, H. Haitjema, B. Van Hooreweder, Texture of inclined up-facing surfaces in laser powder bed fusion of metals, Addit. Manuf. 42 (2021) 101970, https://doi.org/10.1016/j.addma.2021.101970.
[13] G. Kasperovich, R. Becker, K. Artzt, P. Barriobero-Vila, G. Requena, J. Haubrich, The effect of build direction and geometric optimization in laser powder bed fusion of Inconel 718 structures with internal channels, Mater. Des. 207 (2021) 109858, https://doi.org/10.1016/j.matdes.2021.109858.
[14] T. Reiber, J. Rüdesheim, M. Weigold, E. Abele, J. Musekamp, M. Oechsner, Influence of contour scans on surface roughness and pore formation using Scalmalloy® manufactured by laser powder bed fusion (PBF-LB), Mater. Werkst. 52 (4) (2021) 468–481, https://doi.org/10.1002/mawe.202000287.
[15] Z. Ren, D. Wei, S. Wang, D.Z. Zhang, S. Mao, On the role of pre-and post-contour scanning in laser powder bed fusion: thermal-fluid dynamics and laser reflections, Int. J. Mech. Sci. 226 (2022) 107389, https://doi.org/10.1016/j.ijmecsci.2022.107389.
[16] O. Poncelet, M. Marteleur, C. van der Rest, O. Rigo, J. Adrien, S. Dancette, A. Simar, Critical assessment of the impact of process parameters on vertical roughness and hardness of thin walls of AlSi10Mg processed by laser powder bed fusion, Addit. Manuf. 38 (2021) 101801, https://doi.org/10.1016/j.addma.2020.101801.
[17] W. Yuan, H. Chen, T. Cheng, Q. Wei, Effects of laser scanning speeds on different states of the molten pool during selective laser melting: simulation and experiment, Mater. Des. 189 (2020) 108542, https://doi.org/10.1016/j.matdes.2020.108542.
[18] J. Wang, R. Zhu, Y. Liu, L. Zhang, Understanding melt pool characteristics in laser powder bed fusion: an overview of single-and multi-track melt pools for process optimization, Adv. Powder Mater. 2 (4) (2023) 100137, https://doi.org/10.1016/j.apmate.2023.100137.
[19] A. Avanzini, D. Battini, M. Gelfi, L. Girelli, C. Petrogalli, A. Pola, M. Tocci, Investigation on fatigue strength of sand-blasted DMLS-AlSi10Mg alloy, Procedia Struct. Integr. 18 (2019) 119–128, https://doi.org/10.1016/j.prostr.2019.08.146.
[20] A. Pola, D. Battini, M. Tocci, A. Avanzini, L. Girelli, C. Petrogalli, M. Gelfi, Evaluation on the fatigue behavior of sand-blasted AlSi10Mg obtained by DMLS, Frat. Ed. Integrità Strutt. 13 (49) (2019) 775–790, https://doi.org/10.3221/IGF-ESIS.49.69.
[21] J. Damon, S. Dietrich, F. Vollert, J. Gibmeier, V. Schulze, Process dependent porosity and the influence of shot peening on porosity morphology regarding selective laser melted AlSi10Mg parts, Addit. Manuf. 20 (2018) 77–89, https://doi.org/10.1016/j.addma.2018.01.001.
[22] N.E. Uzan, S. Ramati, R. Shneck, N. Frage, O. Yeheskel, On the effect of shot-peening on fatigue resistance of AlSi10Mg specimens fabricated by additive manufacturing using selective laser melting (AM-SLM), Addit. Manuf. 21 (2018) 458–464, https://doi.org/10.1016/j.addma.2018.03.030.
[23] J.G.S. Macías, C. Elangeswaran, L. Zhao, J.Y. Buffière, B. Van Hooreweder, A. Simar, Fatigue crack nucleation and growth in laser powder bed fusion AlSi10Mg under as built and post-treated conditions, Mater. Des. 210 (2021) 110084, https://doi.org/10.1016/j.matdes.2021.110084.
[24] J.G. Santos Macías, L. Zhao, D. Tingaud, B. Bacroix, G. Pyka, C. van der Rest, A. Simar, Hot isostatic pressing of laser powder bed fusion AlSi10Mg: parameter identification and mechanical properties, J. Mater. Sci. 57 (21) (2022) 9726–9740, https://doi.org/10.1007/s10853-022-07027-9.
[25] N.T. Aboulkhair, I. Maskery, C. Tuck, I. Ashcroft, N.M. Everitt, Improving the fatigue behaviour of a selectively laser melted aluminium alloy: influence of heat treatment and surface quality, Mater. Des. 104 (2016) 174–182, https://doi.org/10.1016/j.matdes.2016.05.041.

[26] E. Sert, J. Köppel, M. Butze, F. Brockmann, M. Merkel, A. Öchsner, Determination of the fatigue behaviour of laser powder-bed fused AlSi10Mg specimens using surface and heat treatments, in: Lectures Notes on Advanced Structured Materials, vol. 2, Springer Nature Switzerland, Cham, 2024, pp. 171–189, https://doi.org/10.1007/978-3-031-49043-9_10.

[27] N. Limbasiya, A. Jain, H. Soni, V. Wankhede, G. Krolczyk, P. Sahlot, A comprehensive review on the effect of process parameters and post-process treatments on microstructure and mechanical properties of selective laser melting of AlSi10Mg, J. Mater. Res. Technol. 21 (2022) 1141–1176, https://doi.org/10.1016/j.jmrt.2022.09.092.

[28] J.A.T. Rios, P. Zambrano-Robledo, J.D.T. Taborda, J.A.G. Espinoza, C.J. Isaza, A. Juárez-Hernández, Process parameters effect and porosity reduction on AlSi10Mg parts manufactured by selective laser melting, Int. J. Adv. Des. Manuf. Technol. 129 (7) (2023) 3341–3351, https://doi.org/10.1007/s00170-023-12521-8.

[29] K.V. Yang, P. Rometsch, T. Jarvis, J. Rao, S. Cao, C. Davies, X. Wu, Porosity formation mechanisms and fatigue response in Al-Si-Mg alloys made by selective laser melting, Mater. Sci. Eng. 712 (2018) 166–174, https://doi.org/10.1016/j.msea.2017.11.078.

[30] T. Yang, T. Liu, W. Liao, E. MacDonald, H. Wei, C. Zhang, K. Zhang, Laser powder bed fusion of AlSi10Mg: influence of energy intensities on spatter and porosity evolution, microstructure and mechanical properties, J. Alloys Compd. 849 (2020) 156300, https://doi.org/10.1016/j.jallcom.2020.156300.

[31] N. Sanaei, A. Fatemi, Analysis of the effect of surface roughness on fatigue performance of powder bed fusion additive manufactured metals, Theor. Appl. Fract. Mech. 108 (2020) 102638, https://doi.org/10.1016/j.tafmec.2020.102638.

[32] S. Bagherifard, N. Beretta, S. Monti, M. Riccio, M. Bandini, M. Guagliano, On the fatigue strength enhancement of additive manufactured AlSi10Mg parts by mechanical and thermal post-processing, Mater. Des. 145 (2018) 28–41, https://doi.org/10.1016/j.matdes.2018.02.055.

[33] A. Raja, S.R. Cheethirala, P. Gupta, N.J. Vasa, R. Jayaganthan, A review on the fatigue behaviour of AlSi10Mg alloy fabricated using laser powder bed fusion technique, J. Mater. Res. Technol. 17 (2022) 1013–1029, https://doi.org/10.1016/j.jmrt.2022.01.028.

[34] S. Fini, D. Croccolo, M. De Agostinis, G. Olmi, L. Paiardini, C. Scapecchi, M. Mele, Fatigue response of AlSi10Mg by laser powder bed fusion: influence of build orientation, heat, and surface treatments, Prog. Addit. Manuf. (2024) 1–19, https://doi.org/10.1007/s40964-024-00712-y.

[35] L. Afroz, M. Qian, J. Forsmark, Y. Li, M. Easton, R. Das, Fatigue life of laser powder bed fusion (L-PBF) AlSi10Mg alloy: effects of surface roughness and porosity, Prog. Addit. Manuf. (2024) 1–19, https://doi.org/10.1007/s40964-024-00759-x.

[36] T.D. Piette, A.G. Spangenberger, B.E. Stoner, D.A. Lados, Influence of contour processing parameters on porosity, surface roughness, and fatigue life in laser powder bed Al-10Si-0.4 Mg, J. Manuf. Process. 118 (2024) 419–431, https://doi.org/10.1016/j.jmapro.2024.03.047.

[37] E. Maleki, S. Bagherifard, O. Unal, S. Shao, N. Shamsaei, M. Guagliano, Assessing the efficacy of several impact-based mechanical techniques on fatigue behavior of additive manufactured AlSi10Mg, Mater. Sci. Eng. 872 (2023) 144940, https://doi.org/10.1016/j.msea.2023.144940.

[38] J. Kohout, S. Vĕchet, A new function for fatigue curves characterization and its multiple merits, Int. J. Fatig. 23 (2) (2001) 175–183.

[39] L. Zhao, J.G.S. Macías, L. Ding, H. Idrissi, A. Simar, Damage mechanisms in selective laser melted AlSi10Mg under as built and different post-treatment conditions, Mater. Sci. Eng. 764 (2019) 138210, https://doi.org/10.1016/j.msea.2019.138210.

[40] M. Hamidi Nasab, A. Giussani, D. Gastaldi, V. Tirelli, M. Vedani, Effect of surface and subsurface defects on fatigue behavior of AlSi10Mg alloy processed by laser powder bed fusion (L-PBF), Metals 9 (10) (2019) 1063, https://doi.org/10.3390/met9101063.

[41] B. AlMangour, J.M. Yang, Improving the surface quality and mechanical properties by shot-peening of 17-4 stainless steel fabricated by additive manufacturing, Mater. Des. 110 (2016) 914–924, https://doi.org/10.1016/j.matdes.2016.08.037.

[42] S. Bagehorn, J. Wehr, H.J. Maier, Application of mechanical surface finishing processes for roughness reduction and fatigue improvement of additively manufactured Ti-6Al-4V parts, Int. J. Fatig. 102 (2017) 135–142, https://doi.org/10.1016/j.ijfatigue.2017.05.008.